

On growth, buckling, and rupture of aneurysms

Masoud Hejazi^a, A. Srikantha Phani^{a,*}

^a*Department of Mechanical Engineering, 6250 Applied Science Lane, University of British Columbia, Vancouver, B.C, Canada V6T 1Z4*

Abstract

Aneurysms are localized bulges of arteries, and they can rupture with fatal consequences. Complex mechanobiological factors preclude *in vivo* testing to assess the rupture risk of an aneurysm, and size based criteria are often used in clinical practice to guide surgical interventions. It is often found that tortuous and buckled aneurysms can exceed in size recommended for surgical intervention, and yet do not rupture. This study addresses why buckled aneurysms exhibit this intriguing behaviour by combining *in vitro* inflation experiments on hyperelastic tubes with finite element calculations. Using a biologically relevant material model for an arterial wall, we show that buckled aneurysms can grow in size without rupturing under favourable arterial pre-tensions. Stretch reversal phenomenon exhibited by arteries governs whether buckling or bulging occurs first. Exponential stiffening favours the axial propagation of an aneurysm instead of radial growth in size. The choice of failure criteria based on Ogden's strain energy function, Gent's first stretch invariant, and Cauchy stress are discussed. Failure maps incorporating post bifurcation (bulging and buckling) response are constructed to delineate the regimes of growth, buckling and rupture of an aneurysm.

Keywords: Aneurysm, Buckling, Rupture, Finite Element Analysis

*Corresponding author
phone: +1 (604) 822-6998
fax: +1 (604) 822-2403
email: srikanth@mech.ubc.ca

1. Introduction

An aneurysm is a balloon-like bulge within the wall of a blood vessel, commonly observed in the abdominal and the thoracic regions of aorta, due to local degradation in mechanical properties of an artery (Sakalihasan et al., 2018). Biomechanics of aneurysms has been reviewed in (Vorp, 2007; Sakalihasan et al., 2018), arterial wall modelling in (Holzapfel and Ogden, 2010; Humphrey, 2013; Fung, 2013). An increasing incidence rate of aneurysms, ranging from 5.6 to 10.6 per 100,000 persons/year, has been observed in the past decade in developed countries (Acosta et al., 2006). Mortality rate for a ruptured aortic aneurysm can be up to 90%, especially when it occurs outside of a hospital (Sampson et al., 2014). Hence, estimating the rupture risk for AAAs is critical after an aneurysm is detected. Clinical guidelines rely on the maximum diameter of an aneurysm to estimate the rupture risk (Muluk et al., 2017; Lazaris, 2019). However, some AAAs are found unruptured despite their maximum size exceeding the minimum recommended size (5.5 cm) for surgical interventions (Lazaris, 2019; Fillinger et al., 2004). Tortuous and buckled AAAs whose size far exceed the guidelines have been observed without rupture (Fillinger et al., 2004; Hejazi et al., 2021; Boyd et al., 2016; Ducas et al., 2020; Choi et al., 2021). Arterial stability with aneurysm (Lee et al., 2014) and buckling without aneurysms (Liu et al., 2019) has also been studied, among others. However, the rupture of buckled aneurysms remains to be addressed.

Recently, the hypothesis that buckling offers a fail safe mode for AAAs has been tested through controlled *in vitro* experiments on hyperelastic tubes and numerical modelling (Hejazi et al., 2021) by treating the walls as isotropic and hyperelastic membranes. Pre-tension has been identified as the key factor that governs whether buckling occurs or not. It has been reported that, under low pre-tensions (arterial pre-stress) an aneurysm buckles and grows in size without rupture. Buckling of an aneurysm is shown to arise from the compressive stresses developed outside the bulged region which overcome the arterial pre-tension. Hyperelastic models may be justified on the basis of the degradation of

elastic fibres due to aneurysm’s pathogenesis at incipient rupture (Niestrawska et al., 2019). Bulge formation and other bifurcation phenomena in hyperelastic cylindrical tubes have been studied extensively using approximate membrane theories for thin walled tubes (Haughton and Ogden, 1979b,a; Fu et al., 2012), diffuse interface models (Lestringant and Audoly, 2018, 2020), and for thick walled cylindrical tubes (Fu et al., 2016; Wang and Fu, 2018; Wang et al., 2019; Ye et al., 2020). Hyperelastic models have also been used in finite element calculations (Länne et al., 1992; Gonçalves et al., 2008) to study bulge formation in cylindrical tubes. While a phenomenological and qualitative understanding of aneurysm formation and growth can be obtained using hyperelastic models, they may not be suitable to describe the complex material response of a fiber-reinforced, multi-layered, and anisotropic arterial wall (Holzapfel et al., 2019). Attempts have been made to use more complex material models in finite element calculations (Alhayani et al., 2013; Demirkoparan and Merodio, 2017; Font et al., 2021; Topol et al., 2021; Dehghani et al., 2019). These studies indicate the asymmetry of aneurysm shape (Topol et al., 2021; Font et al., 2021) due to residual stresses, buckling without bulging (Dehghani et al., 2019), competition between radial expansion and axial propagation of a bulge (Alhayani et al., 2014), and the effect of fiber reinforcement on the initiation of the aneurysm (Demirkoparan and Merodio, 2017). However, these computational studies do not address the rupture in the post bulging regime; the role of buckling in preventing it; the influence of arterial pre-tension on the occurrence of buckling, bulging and rupture. Significantly, features such as stretch reversal and exponential stiffening are absent in hyperelastic material models and their influence on aneurysm evolution needs to be clarified.

This study aims to understand the influence of biologically relevant constitutive material laws on the biomechanics of growth and rupture of the abdominal aortic aneurysm (AAA). To do so, we use the Gasser-Ogden-Holzapfel (GOH) constitutive model of arteries (Gasser et al., 2006) to account for exponential stiffening and stretch reversal (Sommer et al., 2010). Experimental protocols and finite element analyses are described in Section 2. Section 3 discusses re-

sults and factors governing the growth and rupture of an aneurysm, culminating in failure maps. Clinical implications and limitations are discussed. Concluding remarks and avenues for further investigation are provided in Section 4.

2. Methodology

We first present the experimental methodology, followed by finite element calculations. Experiments on hyperelastic tube models will be used to validate the finite element methodology, which will then be extended to include biologically relevant material models.

2.1. Experiments on hyperelastic cylindrical tubes

Inflation tests on finite latex rubber (hyperelastic) tubes are conducted as illustrated in Fig. 1. The purpose of these tests is to understand the deformation phenomena of buckling and kinking, and their influence on the axial and radial growth of a bulge. Here, the emphasis is on post bulge regime, and the influence of material models on this regime that has not been investigated in the literature. Material and geometric properties of the tubes used are given in Table. 1. A nominally straight cylindrical rubber tube is fixed at its bottom, and the top end is attached to an Instron (model 5969) tensile tester’s jaw. A known pre-tension (pre-stretch) is applied by moving the jaw upward and then holding it fixed at a prescribed displacement throughout the inflation test. The load cell reads the axial force (F) in this displacement control test. The air inlet is attached to the top end of the tube and a pressure gauge reads the injection pressure. A DSLR camera (Nikon D7000) records the deformation of the tube during air injection and a pressure transducer records the internal pressure. An edge detection algorithm in MATLAB[®] image processing toolbox is used to obtain the bulged profile for further analysis. A number of experiments (39 in total) are performed for different initial pre-tensions, F_i , and aspect ratios by changing the initial lengths of the tube. The initial diameter and the wall thickness are held fixed in all the experiments. Depending on the initial pre-

tension (F_i) two possible outcomes of the inflation tests are shown in Fig. 1(c) and(d), to be discussed later in Section 3.1.

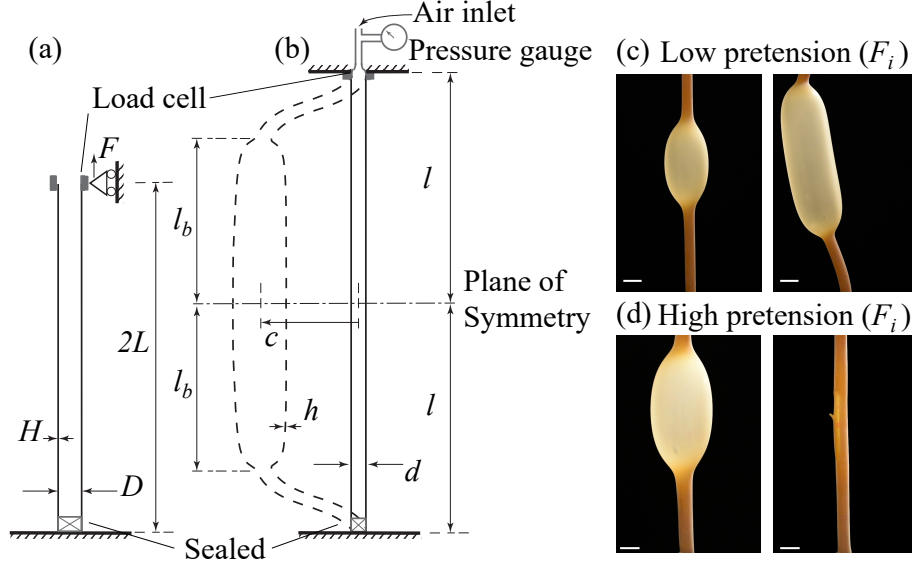


Figure 1: Experimental setup for inflation test of pre-stretched rubber tube with fixed-fixed boundary conditions, L (initial half-length), D (initial diameter), H (initial thickness), F (force applied/measured by Instron), l (stretched half-length), l_b (bulge length), d (deformed diameter), c (buckling amplitude), F_i (longitudinal tension), and h (deformed thickness). (a) Longitudinal tension is applied at the upper end to reach the required pre-stretch (λ_i). (b) Deformed (dashed) and undeformed configurations during inflation subjected to fixed-fixed ends. (c) Bulge initiation and buckling at low longitudinal tension (pre-stretch). (d) Bulge initiation and rupture at high longitudinal tension. The scale bar in white is 2 cm.

2.2. Finite element analyses

Finite element analysis (FEA) offers the ability to systematically vary the material and geometric parameters of the inflation test. We conduct FEA in two parts. In the first part, virtual inflation tests on cylindrical hyperelastic tubes are performed. Initial tension is varied in these simulations. The purpose of these simulations is to verify the experimental observations of buckling in the post bulge regime as well as validate the modelling procedure. In the second part, we use this FEA procedure with a more biologically relevant GOH material

model for the wall.

The FEA has been conducted in three stages. In experiments, all the displacement degrees of freedom have been constrained at the lower end, and at the top end of the tube, as shown in Fig. 1(b). We can exploit symmetry of the boundary conditions by analyzing only one half of the tube. Note that this symmetry still allows the aneurysm to grow radially asymmetric. The top end of the tube with half length, l , as shown in Fig. 1(b), coincides with the crown of the bulge and it is only constrained for the axial displacement to reflect symmetry. The plane of symmetry is also indicated. We use ABAQUS[©] Linear Perturbation Analysis (LPA) and Riks arc length method solvers to obtain the critical bifurcation modes and post bifurcation solution, respectively (Hibbit et al., 2012; Crisfield, 1983). In stage 1 of the FEA, LPA has been performed to obtain the unstable mode shapes of a cylindrical tube subjected to a normalized unit value of prescribed axial stretch and internal pressure. The global nodal imperfection has been introduced based on the first two circumferential modes (global bulge shape) and the first axial mode. It should be noted that due to manufacturing defects, these imperfections naturally exist in the tubes subjected to the inflation test in Section 2.1. In stage 2, the desired pre-stretch is applied and held constant for various prescribed values, identical to that in experiments on rubber tubes. Finally, the inflation test is simulated by increasing the internal pressure. Both stages 2 and 3 use Riks method.

Linear shell elements with reduced integration (S4R) were used (Hibbit et al., 2012). We used 31 elements for the circumference and 199 elements along the length of the tube (6169 total). Element size and amplitude of imperfection are two important simulation parameters for the bifurcation analysis. For the Riks method, global nodal imperfection of order of 10^{-3} , normalized with respect to element size, has been introduced for the first two circumferential modes (global bulge shape) and the first axial mode (buckling mode). The number of elements and the normalized (with respect element size) modal amplitude of imperfection (10^{-3}) have been chosen based on the convergence of the critical pressure associated with bulging instability.

2.3. Material models

Two material models are considered in the finite element analyses: isotropic hyperelastic wall material and anisotropic GOH model. For the hyperelastic model, we use two failure criteria, respectively based on Ogden's strain energy function (SEF) and Gent's criterion based on the first stretch invariant. For the GOH model we Cauchy stress based failure criterion following (Sherifova and Holzapfel, 2019).

The Ogden' SEF (W_O) for a cylindrical coordinate with plane stress can be expressed as

$$W_O = \sum_{i=1}^3 \frac{s_i}{\alpha_i} (\lambda_1^{\alpha_i} + \lambda_2^{\alpha_i} + \lambda_3^{\alpha_i} - 3), \quad (1)$$

$$\lambda_1 = \lambda_z, \lambda_2 = \lambda_\theta, \lambda_3 = (\lambda_z \lambda_\theta)^{-1},$$

where (λ_z and λ_θ) are principal stretches in cylindrical coordinate system for an axisymmetric membrane. The material parameters are given in Table. 1 based on our previous experimental calibration (Hejazi et al., 2021). We used two different rupture criteria: (1) The maximum strain energy density based on Ogden's model in Eq. (1); (2) the maximum in-plane first stretch invariant based on Gent's material model (Gent, 1996), which reads

$$I = \lambda_1^2 + \lambda_2^2 + \lambda_3^2 - 3, \quad (2)$$

$$\lambda_1 = \lambda_z, \lambda_2 = \lambda_\theta, \lambda_3 = (\lambda_z \lambda_\theta)^{-1}.$$

First, we use the calibrated material parameters for Ogden's strain energy function (SEF) in Eq. (1) to validate our FEA with experiments. Next, with identical assumptions as above, namely, axisymmetric membrane and plane stress, the Gasser-Ogden-Holzapfel (GOH) model's SEF (W_H) can be expressed as

$$W_H = \frac{c_{10}}{2} (I_1 - 3) + \frac{k_1}{k_2} (\exp[k_2(\kappa I_1 + (1 - 3\kappa)I_4 - 1)] - 1), \quad (3)$$

$$I_1 = \lambda_z^2 + \lambda_\theta^2 + (\lambda_z \lambda_\theta)^{-2}, \quad I_4 = \lambda_z^2 \sin^2 \gamma + \lambda_\theta \cos^2 \gamma,$$

where, c_{10} , k_1 , and k_2 are the material parameters regarding the contribution of strain energy in the matrix and fibers. The structural parameters are κ and γ represent the in-plane fiber gaussian distribution and fiber orientation with

respect to circumferential direction (θ), respectively (Gasser et al., 2006). The first term in the above equation containing c_{10} can represent the strain energy stored in the extra cellular matrix and the second term is the strain energy stored in reinforcing fibers (collagen). k_1 and k_2 respectively correspond to the volume fraction and stiffness of collagen fibers. The parameters used in the computations are given in Table. 1 baed on *ex-vivo* calibration test on AAA tissue samples (Niestrawska et al., 2019).

Table 1: Geometric and material properties of the tubes in experiment and FEA based on Eq. (1) and Eq. (3)

Internal diameter, D	6.5 mm
Length, $2L$	10 - 20 cm
Tube wall thickness, H	1.5 mm
Ultimate uniaxial stretch, λ_{ut}	7.85 ± 0.8
Ogden's SEF parameters	$\alpha_1 = 1.04; \alpha_2 = 1.33; \alpha_3 = 4.46$ $s_1 = 704.8; s_2 = 373.2; s_3 = 2.8$ (s_i in kPa)
GOH's SEF parameters	$c_{10} = 5.9$ kPa; $k_1 = 18.2$ kPa; $k_2 = 17.7$ $\kappa = 0.242; \gamma = 60^\circ$

3. Results and discussion

In this section we first validate the FEA modelling procedure by comparing it with experiments and then use the FEA subsequently for different material models, geometric parameters, and pre-tensions.

3.1. Rubber tube: modeling and experiments

With fixed-fixed boundary conditions, a pre-stretched tube subjected to internal pressure undergoes three stages of deformation as shown in Fig. 2(a): (1) uniform expansion, (2) radial expansion and axial growth of the aneurysm, (3) buckling and/or rupture. During the uniform expansion, the internal pressure increases monotonically until a global long-wavelength bulge forms with a

relatively small amplitude. The formation of the long-wavelength bulge is associated with a reduction of pressure and it rapidly localizes forming the so-called aneurysm, or a bulge. Formation of the localized bulge leads to a sudden pressure relaxation. As the bulge region invades the straight portions of the tube, the axial force drops due to load relaxation. A compressive region forms outside the bulged region, since both ends are constrained, lateral buckling occurs. If the pre-stretch is high enough the tube may rupture without buckling. This is because the decrease in axial force due to an axially propagating bulge is insufficient to overcome the pre-tension. For the case where buckling follows bulge formation, as shown in Fig. 2(a), the pressure-force curves show a good agreement between the experiments and the FEA. The FEA shows a slightly stiffer response due to slight differences in the material properties and discretization. In the post buckling regime, shown in Fig. 2(b), the normalized buckling amplitude ratio (c/d) versus bulge length fraction (l_b/l) plot shows a similar level of agreement. In the early stages of buckling, the lateral displacement increases rapidly, but with the increasing buckling amplitude (c), we observe a hardening behaviour that leads to a plateau (indicated by 3 in Fig. 2(b)) in FEA. This deviation arises from the formation of a localized kink at the bottom end and the neck of the bulge (See Fig. 2(c)). Compared to FEA, the kink observed in the experiment, see Fig. 2(d), is not as strong. Having verified the validity of FEA, we now can vary material model and other parameters.

The effect of pre-stretch on the progression of the buckling and bulge growth is shown in Fig. 3. Here, the normalized buckling amplitude is plotted against the fraction of the length of the tube, l_b/l , occupied by the bulge. With larger axial propagation, the uniform section of the tube becomes shorter, and the end kink has a more predominant effect on hardening transition in buckling amplitude development (see the transition region in Fig. 3(a)). The axial and radial propagation of a bulge is shown in Fig. 3(b). At the onset of bulge propagation, the uniform expansion is followed by the formation of a long-wavelength bulge, which then becomes localized by growing in radial size. The radial propagation of the localized bulge gradually turns into axial propagation

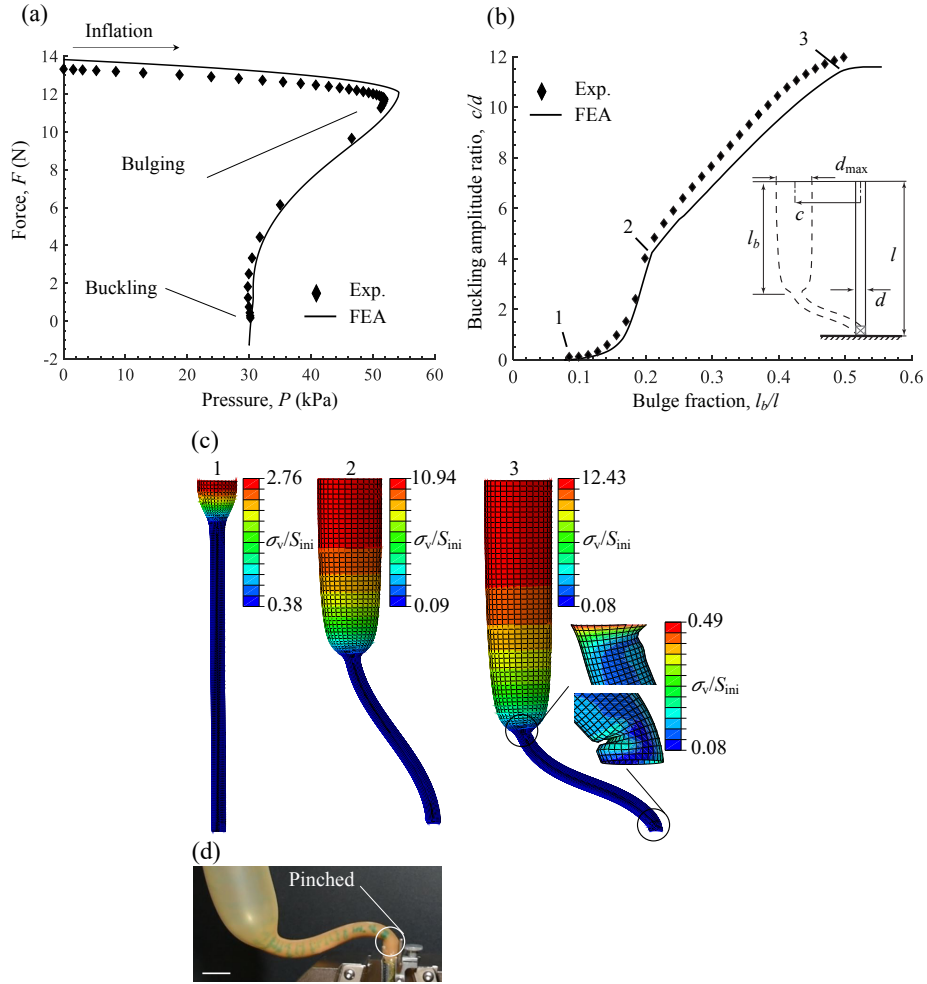


Figure 2: Finite element analysis versus experiments on hyperelastic tubes. (a) Longitudinal force versus internal pressure during inflation. The onset of bulging and buckling are associated with a drop in the internal pressure and a drop in the longitudinal force, respectively. (b) Buckling amplitude growth versus bulge axial growth showing three regimes: (1-2) buckling initiation, (2-3) flexural stiffening due to bulge axial growth and reduction in length of uniform section, (3-end) buckling amplitude limited by local kinking. (c) FEA stress distribution associated with points 1 to 3 in (b) and shear stress at the neck of the the bulge and bottom fixed end subjected to kink. (d) Small kink formation at the bottom fixed end of the tube during experiment.

until the buckling sets in. With buckling, the radial propagation declines and the bulge length development accelerates (Fig. 3(b)). This behaviour is a result of relaxation of axial force due to buckling, which allows the bulge to easily propagate along the length of the tube. However, with a higher pre-stretch, the bulge needs to invade longer until the buckling (and hence relaxation) develops. This means that the onset of buckling is delayed in Fig. 3(b).

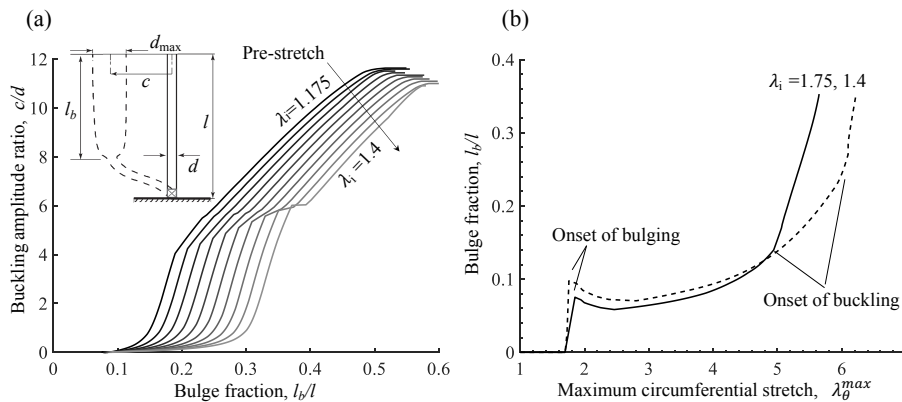


Figure 3: Effect of longitudinal pre-stretch on the growth of l_b (axial length of the bulge) and c (buckling amplitude); $\lambda_{\theta}^{\max} = d_{\max}/d$. (a) By increasing tension, buckling initiation requires larger bulge length and flexural stiffening is more significant due to a shorter length of the uniform section. (b) The long wave bulge profile ($l_b/l < 0.1$) is followed by localized bulge formation and rapid axial growth due to buckling. With higher longitudinal pre-stretch the length of the long wave is larger and the buckling initiates at larger diameter/circumferential stretch.

A rupture portrait based on buckling amplitude ratio (c/d) and maximum circumferential stretch ($\lambda_{\theta}^{\max} = d_{\max}/d$) is shown in Fig. 4(a). Two rupture criteria, of Ogden and Gent, are compared. Using FEA, we first obtained the Gent's first invariant stretch, Eq. (2), and Ogden's SEF, Eq. (1), for all the data points throughout the inflation of the tube with different pre-stretch values ($1.75 \leq \lambda_i \leq 1.4$). Then, the contour lines, shown in Fig. 4(a), have been obtained for all the data points to delineate the safe-unsafe boundary with respect to rupture. Along these curves the pre-stretch varies as indicated in Fig. 4(a). By increasing the pre-stretch, the buckling amplitude falls as well as the max-

imum circumferential stretch. With a large enough pre-stretch (initial tension, F_i), rupture without buckling (see the diamond data points in Fig. 4(b)) occurs. Analytical buckling and rupture envelopes are obtained by following (Hejazi et al., 2021). A modified post-buckling rupture line based on FEA is shown for both Gent's stretch invariant and Ogden's strain energy density based on the contour lines in Fig. 4(a). At higher values of pre-stretch, Ogden's criterion is conservative, and at lower pre-stretch values Gent's criterion is conservative. This is due to the additional tensile strain energy induced by buckling.

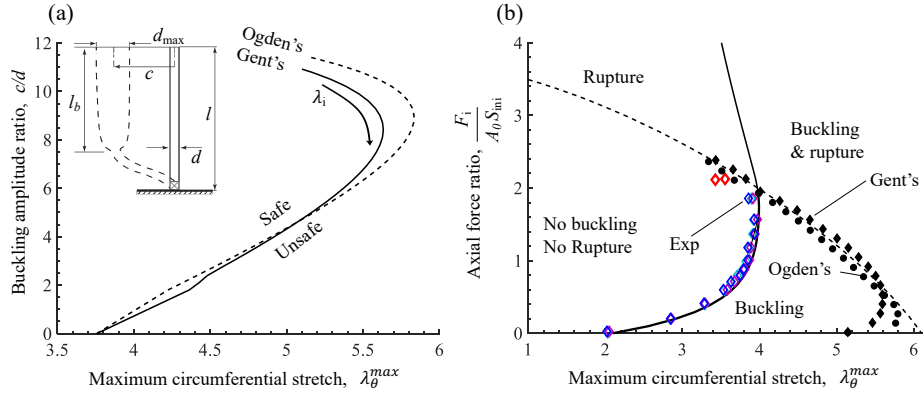


Figure 4: Rupture behaviour of the rubber tube subjected to an internal pressure and fixed longitudinal pre-stretch, F_i (longitudinal tension at the beginning of the inflation), A_0 (tube cross section area in deformed configuration). (a) Rupture contour line in the plane of buckling amplitude and maximum circumferential stretch based on Ogden's maximum strain energy density and Gent's maximum stretch invariant. (b) Rupture and buckling phase portrait showing the effect of pre-stretch and buckling on the rupture behaviour.

3.2. GOH material model

We implemented the GOH material model from Eq. (3) with the parameters for the control case are given in Table. 1.

Comparing the inflation tests on a GOH tube shown in Fig. 5(a) with Fig. 2(a) for a hyperelastic tube, it can be observed that the decrease in pressure after the formation of the aneurysm is less pronounced for GOH. Hence, the propagation pressure for the aneurysm to spread along the length of the artery is lower. The

two instability modes, bulging and buckling can be identified in the pressure-force curve in Fig. 5(b). Sudden drops in pressures and axial force follow the bulging and buckling, respectively.

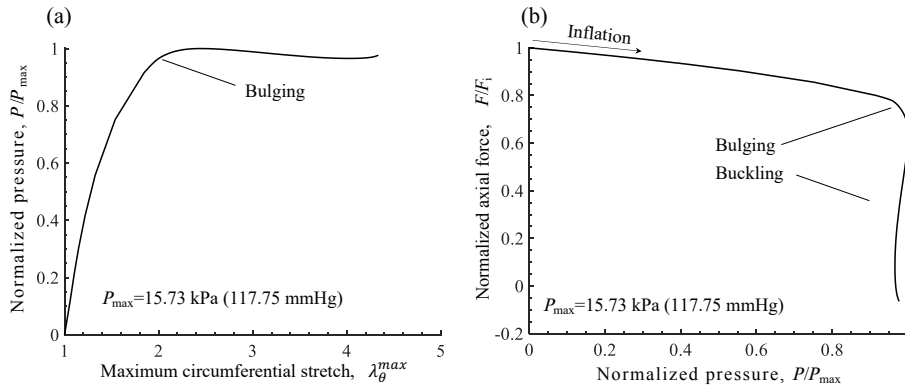


Figure 5: Inflation of a tube with arterial material properties based on fiber reinforced hyper-elastic GOH model, showing the onset of bulging and buckling. (a) In contrast to a rubber tube, the internal pressure drop after bulge formation is not significant during the propagation phase. (b) The pressure-force curve shows the onset of bulging (softening behaviour of the pressure (P)) and onset of buckling (significant drop in the axial force (F)). Here, buckling follows the formation of the aneurysm.

A 3D bifurcation map for the tube with the aortic wall is shown in Fig. 6(a). In GOH model, compressive forces may arise in the straight regions of the tube without a bulge formation due to stretch inversion. Buckling before bulging can occur, which is not possible in a hyperelastic tube. In Fig. 6(b), we can see a small drop in the pressure as the indicator of the bulge formation and an immediate increase in buckling amplitude indicating the lateral buckling. By comparing two different cases with small ($\lambda_i = 1.15$) and large ($\lambda_i = 1.4$) pre-stretches, we see how the order of bulging and buckling may reverse (see also FEA results in Fig. 6(c) and (d)).

The growth rate of an AAA is one of the important factors in clinical decision making. Here, we investigated the axial and radial growth and the effect of buckling on these two parameters. Fig. 7(a) shows the progression of the buckling amplitude (c) versus the bulge radial growth (λ_θ^{\max}). We see both cases of

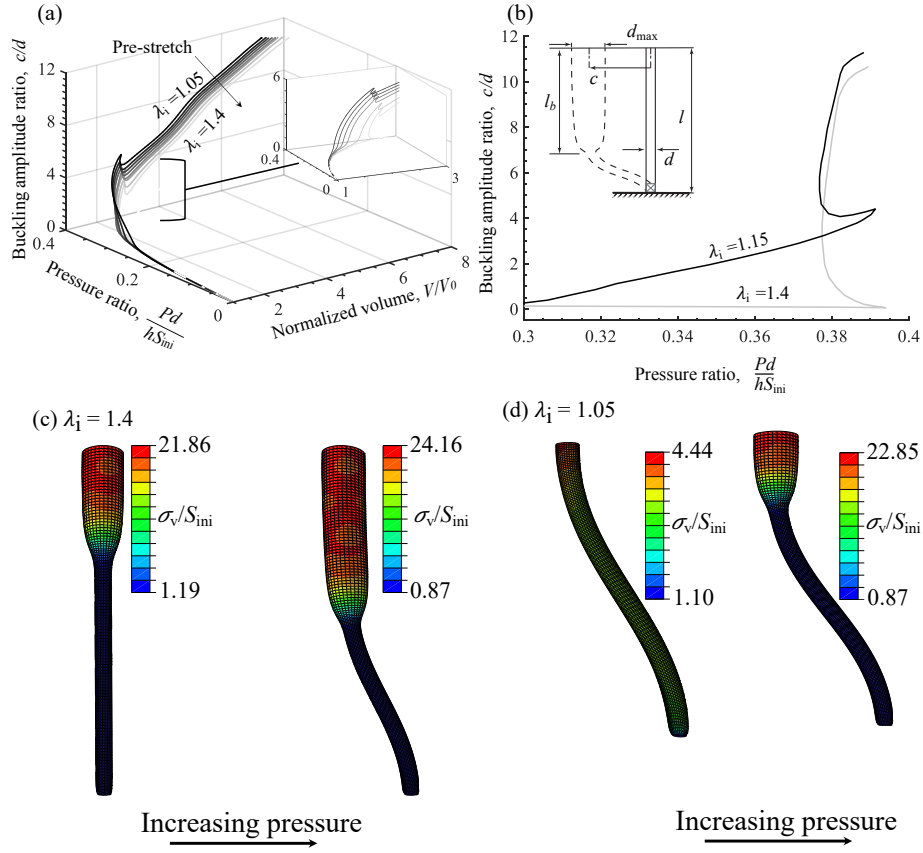


Figure 6: Arterial tube buckling and bulging bifurcation points (limit point instabilities) in the plane of inflation volume versus internal pressure: P (internal pressure), V (internal volume), V_0 (internal volume at the beginning of inflation), $S_{ini} = \frac{1}{2} \left[\frac{\partial}{\partial \lambda_\theta} \left(\frac{\partial W}{\partial \lambda_z} \right) \right]$ is the initial shear modulus. (a) The bulge and buckling initiation are evident by increase in $(c/d$ and limit point instability of Pd/hS_{ini} . (b) The effect of tension on the buckling and bulge initiation indicates that with lower pre-stretch tube may buckle before bulge initiation, but as the pre-stretch increases, bulge forms before buckling. Similar to rubber tubes, the propagation pressure does not change due to a change in the pre-stretch. (c) Post bulge buckling of the arterial tube with high pre-stretch. (d) Post buckling bulge of the arterial tube with low pre-stretch.

post bulge buckling ($\lambda_i = 1.15$) and post-buckling bulge ($\lambda_i = 1.4$). In both cases, the initial stage of the buckling is associated with a surge in amplitude (c), followed by a small decrease, and another increase of the amplitude. The

buckling and long-wavelength bulge initiate concurrently at the early stages. By the formation of the localized bulge, the buckling amplitude declines slightly, followed by significant radial growth of the bulge. With the transition of radial growth into axial propagation, the buckling amplitude increases further until it reaches the hardening as a result of the reduction in uniform length and pinching effects at the end. Also, with a longer bulge length, the maximum diameter tends to shrink as a result of relaxation of the axial force due to buckling. The axial propagation of the bulge (l_b) is shown in Fig. 7(b). In the first stage, we see the formation of the long-wavelength bulge. The formation of the localized bulge results in a minor reduction in the bulge length (l_b) and a significant increase in radial size. In the next stage of the propagation, the maximum radial size approximately remains constant (marginal reduction is observed) while the bulge propagates axially.

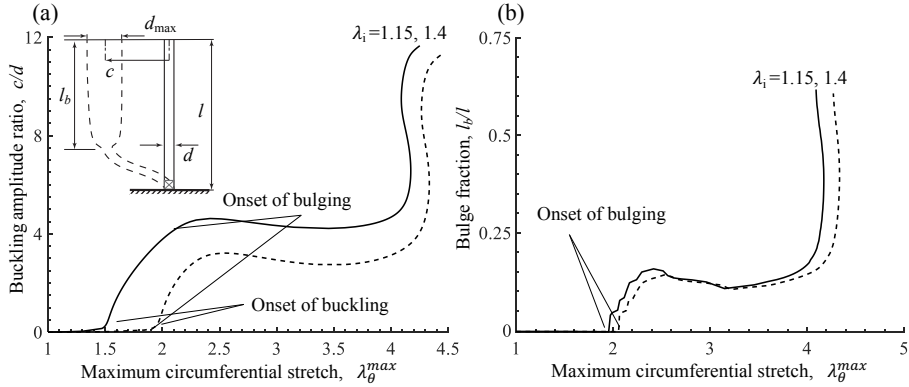


Figure 7: Growth of a bulge in an arterial tube. $\lambda_{\theta}^{max} = d_{max}/d$ (radial size), l_b/l (axial size), c/d (lateral buckling growth). (a) Buckling before ($\lambda_i = 1.15$) and after ($\lambda_i = 1.4$) bulge formation. The buckling amplitude (c) slightly reduces during propagation phase due to stress relaxation in the uniform section. (b) Initial bulge with a long wave length transforms into a localized bulge and results in a slight reduction in the bulge length (l_b). At the late stages of propagation, the axial growth takes over radial growth.

Finally, the rupture map of a tube with the aortic wall with GOH material model, subjected to axial pre-tension and internal pressure is shown in Fig. 8(a). By reducing the c_{10} and increasing k_1 , we can model the elastin degradation,

which is commonly observed for AAAs (Niestrawska et al., 2019). We showed two rupture thresholds by changing these parameters (c_{10} , k_1) parameter in the SEF function. The rupture criterion is based on the maximum Cauchy stress, which is located at the crown of the bulge on the outer wall with respect to buckling curvature. Similar to Fig. 4(a), we obtained the failure points using FEA for various pre-stretch values and sketched the failure boundary on buckling amplitude-circumferential stretch plot. Both of these parameters are easy to measure using common imaging techniques in clinical practice (e.g. CT scans and ultrasound). The control case has a qualitatively similar failure envelope compared to the hyperelastic tube in Fig. 4(a). With a larger buckling amplitude for low pre-tension tubes, a smaller circumferential stretch is needed for rupture to occur. However, in general, buckling acts as a fail safe mode, and postpones rupture. When buckling occurs, rupture takes place at a much larger size of the aneurysm, as shown in Fig. 8(a). The exponential stiffening is more pronounced at lower values of c_{10} and higher values of k_1 , which prevents the radial growth of the aneurysm and favours buckling. This is also evident in Fig. 8(b) which shows higher amplitudes of buckling (lower size of aneurysm) for decreasing c_{10} and increasing k_1 .

3.3. Clinical implications

In this study, we showed two mechanisms that may govern the arterial buckling. The first one, buckling without bulge, is a result of stretch inversion, which is sensitive to microscopic fiber orientation and composition. The second mechanism, probably more relevant to AAAs, is the formation of the compressive force due to axial propagation of the aneurysm. It is not clear whether the buckling always follows the bulge or vice versa. However, many AAAs are commonly observed in a buckled state (Fillinger et al., 2004; Ducas et al., 2020; Hejazi et al., 2021) do not rupture at a much larger size (Choi et al., 2021). This study suggests that a straight aneurysm has a higher risk of rupture compared to a buckled aneurysm.

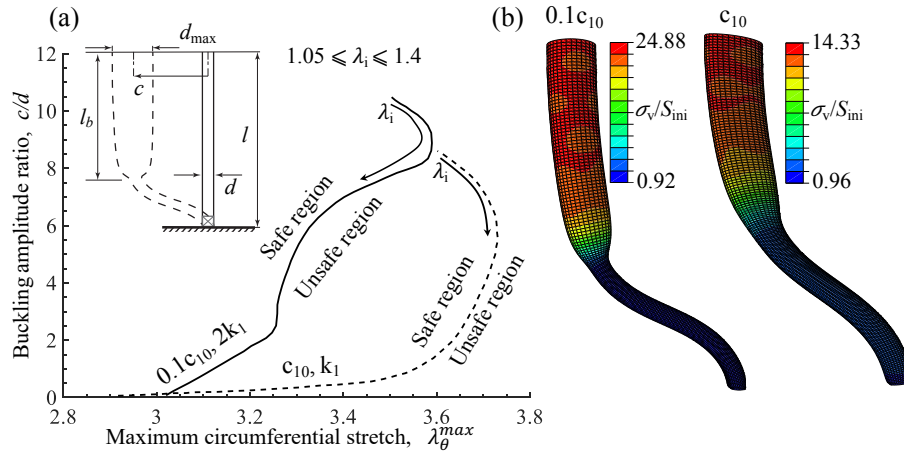


Figure 8: Rupture map for an arterial tube. (a) The effect of material parameters on the rupture of bulged-buckled arterial tube in the plane of maximum radial size and buckling amplitude. (b) Corresponding stress distribution figures for the rupture contours in (a).

3.4. Limitations

There are limitations of this study. The most significant is the lack of haemodynamics and fluid-structure interactions. Such formidable calculations need to be attempted in the future, specially when the artery undergoes a structural instability like buckling. Arterial branches and the curvature imposed by spine posterior support are not considered. Nonetheless, the rupture maps for both the rubber tube and the tube with an aortic wall can provide useful information regarding the rupture of tortuous AAAs by correlating the 2D buckling amplitude and maximum diameter to the rupture risk. We anticipate such studies in the future.

4. Conclusion

We performed a series of inflation tests on rubber tubes with axial pre-tension under fixed-fixed boundary conditions. We performed finite element calculations using ABAQUS[®] commercial solvers including linear perturbation analysis and Riks method solver. The FEA code has shown reasonable agreement with *in vitro* experiments on hyperelastic rubber tubes. With a validated FEA code,

we implemented the properties of the aortic wall using fiber-reinforced hyperelastic material with collagen and elastin fibers. We investigated the bulging and buckling instabilities, and explored the bulge growth and rupture in post bulge/buckling regime. We implemented different AAA pathogenesis scenarios by changing the material parameters associated with fiber deposition and degradation. We presented a rupture map in the plane of buckling amplitude plotted against maximum circumferential stretch, both of which can be measured using 2D clinical images (CT and ultrasound) with minimal technical requirements (e.g. 3D image reconstruction). We concluded that the post bulge buckling is a protective mechanism against rupture.

Acknowledgment

We gratefully acknowledge the funding provided for this research by the National Science and Engineering Research Council of Canada (NSERC) through Discovery Grant. Discussions with Prof. Y. Hsiang from the Vancouver General Hospital are thankfully acknowledged.

References

- Acosta, S., Ögren, M., Bengtsson, H., Bergqvist, D., Lindblad, B., Zdanowski, Z., 2006. Increasing incidence of ruptured abdominal aortic aneurysm: a population-based study. *Journal of vascular surgery* 44, 237–243.
- Alhayani, A., Giraldo, J., Rodríguez, J., Merodio, J., 2013. Computational modelling of bulging of inflated cylindrical shells applicable to aneurysm formation and propagation in arterial wall tissue. *Finite elements in analysis and design* 73, 20–29.
- Alhayani, A., Rodríguez, J., Merodio, J., 2014. Competition between radial expansion and axial propagation in bulging of inflated cylinders with application to aneurysms propagation in arterial wall tissue. *International journal of engineering science* 85, 74–89.

- Boyd, A.J., Kuhn, D.C., Lozowy, R.J., Kulbisky, G.P., 2016. Low wall shear stress predominates at sites of abdominal aortic aneurysm rupture. *Journal of vascular surgery* 63, 1613–1619.
- Choi, S.H., Hejazi, M., Phani, S.A., Hsiang, Y., 2021. Evaluation of aortic tortuosity as a negative predictor of abdominal aortic aneurysm rupture, in: 2021 Vascular annual meeting, (SVS).
- Crisfield, M., 1983. An arc-length method including line searches and accelerations. *International journal for numerical methods in engineering* 19, 1269–1289.
- Dehghani, H., Desena-Galarza, D., Jha, N., Reinoso, J., Merodio, J., 2019. Bifurcation and post-bifurcation of an inflated and extended residually-stressed circular cylindrical tube with application to aneurysms initiation and propagation in arterial wall tissue. *Finite elements in analysis and design* 161, 51–60.
- Demirkoparan, H., Merodio, J., 2017. Bulging bifurcation of inflated circular cylinders of doubly fiber-reinforced hyperelastic material under axial loading and swelling. *Mathematics and Mechanics of Solids* 22, 666–682.
- Ducas, A.A., Kuhn, D.C., Bath, L.C., Lozowy, R.J., Boyd, A.J., 2020. Increased matrix metalloproteinase 9 activity correlates with flow-mediated intraluminal thrombus deposition and wall degeneration in human abdominal aortic aneurysm. *Journal of vascular surgery: vascular science* 1, 190–199.
- Fillinger, M.F., Racusin, J., Baker, R.K., Cronenwett, J.L., Teutelink, A., Schermerhorn, M.L., Zwolak, R.M., Powell, R.J., Walsh, D.B., Ruzicidlo, E.M., 2004. Anatomic characteristics of ruptured abdominal aortic aneurysm on conventional ct scans: implications for rupture risk. *Journal of vascular surgery* 39, 1243–1252.
- Font, A., Jha, N.K., Dehghani, H., Reinoso, J., Merodio, J., 2021. Modelling

- of residually stressed, extended and inflated cylinders with application to aneurysms. *Mechanics research communications* 111, 103643.
- Fu, Y., Liu, J., Francisco, G., 2016. Localized bulging in an inflated cylindrical tube of arbitrary thickness—the effect of bending stiffness. *Journal of the mechanics and physics of solids* 90, 45–60.
- Fu, Y.B., Rogerson, G.A., Zhang, Y.T., 2012. Initiation of aneurysms as a mechanical bifurcation phenomenon. *International journal of non-linear mechanics* 47, 179–184.
- Fung, Y.c., 2013. *Biomechanics: mechanical properties of living tissues*. Springer Science & Business Media.
- Gasser, T.C., Ogden, R.W., Holzapfel, G.A., 2006. Hyperelastic modelling of arterial layers with distributed collagen fibre orientations. *Journal of the royal society interface* 3, 15–35.
- Gent, A.N., 1996. A new constitutive relation for rubber. *Rubber chemistry and technology* 69, 59–61.
- Gonçalves, P.B., Pamplona, D., Lopes, S.R.X., 2008. Finite deformations of an initially stressed cylindrical shell under internal pressure. *International journal of mechanical sciences* 50, 92–103.
- Haughton, D., Ogden, R., 1979a. Bifurcation of inflated circular cylinders of elastic material under axial loading—ii. exact theory for thick-walled tubes. *Journal of the mechanics and physics of solids* 27, 489–512.
- Haughton, D.M., Ogden, R.W., 1979b. Bifurcation of inflated circular cylinders of elastic material under axial loading—i. membrane theory for thin-walled tubes. *Journal of the mechanics and physics of solids* 27, 179–212.
- Hejazi, M., Hsiang, Y., Srikantha Phani, A., 2021. Fate of a bulge in an inflated hyperelastic tube: theory and experiment. *Proceedings of the royal society A: mathematical, physical and engineering sciences* 477, 20200837.

- Hibbit, H., Karlsson, B., Sorensen, E., 2012. Abaqus user manual, version 6.12. Simulia, providence, RI 545.
- Holzapfel, G.A., Ogden, R.W., 2010. Constitutive modelling of arteries. *Proceedings of the royal society A: mathematical, physical and engineering sciences* 466, 1551–1597.
- Holzapfel, G.A., Ogden, R.W., Sherifova, S., 2019. On fibre dispersion modelling of soft biological tissues: a review. *Proceedings of the royal society A: mathematical, physical and engineering sciences* 475, 20180736.
- Humphrey, J.D., 2013. *Cardiovascular solid mechanics: cells, tissues, and organs*. Springer Science & Business Media.
- Länne, T., Sonesson, B., Bergqvist, D., Bengtsson, H., Gustafsson, D., 1992. Diameter and compliance in the male human abdominal aorta: influence of age and aortic aneurysm. *European journal of vascular surgery* 6, 178–184.
- Lazaris, A.M., 2019. Regarding “the society for vascular surgery practice guidelines on the care of patients with an abdominal aortic aneurysm”. *Journal of vascular surgery* 69, 975.
- Lee, A.Y., Sanyal, A., Xiao, Y., Shadfan, R., Han, H.C., 2014. Mechanical instability of normal and aneurysmal arteries. *Journal of biomechanics* 47, 3868–3875.
- Lestringant, C., Audoly, B., 2018. A diffuse interface model for the analysis of propagating bulges in cylindrical balloons. *Proceedings of the royal society A: mathematical, physical and engineering sciences* 474, 0313–0333.
- Lestringant, C., Audoly, B., 2020. Asymptotically exact strain-gradient models for nonlinear slender elastic structures: a systematic derivation method. *Journal of the mechanics and physics of solids* 136, 103730.
- Liu, Y., Ye, Y., Althobaiti, A., Xie, Y.X., 2019. Prevention of localized bulging in an inflated bilayer tube. *International journal of mechanical sciences* 153, 359–368.

- Muluk, S.L., Muluk, P.D., Shum, J., Finol, E.A., 2017. On the use of geometric modeling to predict aortic aneurysm rupture. *Annals of vascular surgery* 44, 190–196.
- Niestrawska, J.A., Regitnig, P., Viertler, C., Cohnert, T.U., Babu, A.R., Holzapfel, G.A., 2019. The role of tissue remodeling in mechanics and pathogenesis of abdominal aortic aneurysms. *Acta biomaterialia* 88, 149–161.
- Sakalihan, N., Michel, J.B., Katsargyris, A., Kuivaniemi, H., Defraigne, J.O., Nchimi, A., Powell, J.T., Yoshimura, K., Hultgren, R., 2018. Abdominal aortic aneurysms. *Nature reviews disease primers* 4, 1–22.
- Sampson, U.K., Norman, P.E., Fowkes, F.G.R., Aboyans, V., Song, Y., Harrrell Jr, F.E., Forouzanfar, M.H., Naghavi, M., Denenberg, J.O., McDermott, M.M., et al., 2014. Estimation of global and regional incidence and prevalence of abdominal aortic aneurysms 1990 to 2010. *Global heart* 9, 159–170.
- Sherifova, S., Holzapfel, G.A., 2019. Biomechanics of aortic wall failure with a focus on dissection and aneurysm: a review. *Acta biomaterialia* 99, 1–17.
- Sommer, G., Regitnig, P., Költringer, L., Holzapfel, G.A., 2010. Biaxial mechanical properties of intact and layer-dissected human carotid arteries at physiological and supraphysiological loadings. *American journal of physiology-heart and circulatory physiology* 298, H898–H912.
- Topol, H., Al-Chlahawi, M.J., Demirkoparan, H., Merodio, J., 2021. Bulging initiation and propagation in fiber-reinforced swellable mooney–rivlin membranes. *Journal of engineering mathematics* 128, 1–15.
- Vorp, D.A., 2007. Biomechanics of abdominal aortic aneurysm. *Journal of biomechanics* 40, 1887–1902.
- Wang, J., Fu, Y., 2018. Effect of double-fibre reinforcement on localized bulging of an inflated cylindrical tube of arbitrary thickness. *Journal of engineering mathematics* 109, 21–30.

- Wang, S., Guo, Z., Zhou, L., Li, L., Fu, Y., 2019. An experimental study of localized bulging in inflated cylindrical tubes guided by newly emerged analytical results. *Journal of the mechanics and physics of solids* 124, 536–554.
- Ye, Y., Liu, Y., Fu, Y., 2020. Weakly nonlinear analysis of localized bulging of an inflated hyperelastic tube of arbitrary wall thickness. *Journal of the mechanics and physics of solids* 135, 103804.